Research Square

Preprints are preliminary reports that have not undergone peer review.
They should not be considered conclusive, used to inform clinical practice,
or referenced by the media as validated information.

Hot cracking in high strength carbon steel weld joints

Kyutae Han

kthan99@posco.com

POSCO Global R&D Center https://orcid.org/0000-0002-9561-2004

Seunggab Hong

POSCO Global R&D Center

Younghwan Park

POSCO Global R&D Center

Research Article

Keywords: Steel plate for shipbuilding, Steel plate for wind tower and substructure, Submerged arc welding, Gas tungsten arc welding, Varestraint test, Hot cracking, Solidification cracking.

Posted Date: November 26th, 2026

DOI: https://doi.org/10.21203/rs.3.rs-11599535/v1

License: This work is licensed under a Creative Commons Attribution 4.0 International License.
Read Full License

IX-L-1317-2026

Hot cracking in high-strength carbon steel weld joints

K. Han*, Y. Park, S. Hong

Technical Research Laboratories, POSCO
*kthan99@posco.com, 0000-0002-9561-2004

Abstract

In the present study, the hot cracking susceptibility of the submerged arc weld metal in steel plates for the shipbuilding and wind tower industries was investigated. The susceptibility was predominantly determined by the chemical composition of the fusion zone, particularly the carbon, phosphorus, and sulfur contents. The weld metal composition was governed by the wire and flux compositions, flux basicity, and the extent of base metal dilution. Transverse Varestraint tests were performed to quantitatively analyze the cracking behavior, determine the weld metal compositions required to prevent hot cracking, and identify the optimum welding consumables for each steel grade. The effects of alloying elements and impurity contents on hot cracking susceptibility were investigated by comparing the brittle temperature range (BTR) obtained from the Varestraint tests with thermodynamic calculations of solidification behavior as a function of weld metal composition.

Keywords

Steel plate for shipbuilding, Steel plate for wind tower and substructure, Submerged arc welding, Gas tungsten arc welding, Varestraint test, Hot cracking, Solidification cracking.

1. Introduction

Generally, weld cracking can be broadly classified into hot cracking and cold cracking based on the initiation temperature. Hot cracking, which occurs at elevated temperatures within the weld metal or the heat-affected zone (HAZ), is initiated during or immediately after welding. It is driven by the synergistic effects of solidification shrinkage of the liquid phase, tensile stresses induced by external constraints, and the presence

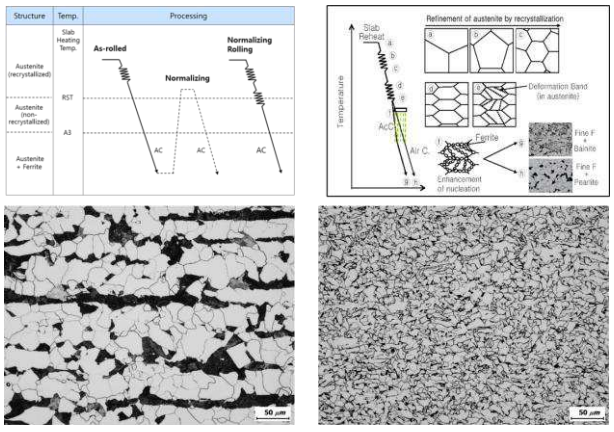
of crack-sensitive microstructures. Specifically, the causes of hot cracking can be categorized into procedural factors, such as weld bead geometry and constraint conditions, and metallurgical factors. Metallurgical factors are primarily attributed to the formation of low-melting-point compounds resulting from the segregation of impurity elements such as phosphorus (P) and sulfur (S). Because the solubility of these impurities varies significantly depending on the primary solidification phase, controlling the solidification mode is of paramount importance. The solidification mode of the metal exerts a profound influence on various hot cracking phenomena in weldments [1-2]. It governs not only the segregation behavior of impurities but also the grain size. In the mushy zone, it affects the solidification temperature range and the back-healing capability of the eutectic liquid, thereby directly influencing solidification cracking. Furthermore, it affects liquation cracking by altering the continuity of eutectic constituents in the partially melted zone (PMZ) of the HAZ and the grain coherency between the fusion zone and the HAZ. Additionally, it influences ductility dip cracking (DDC) which occurs in the HAZ within the temperature range between approximately half the melting temperature and the dynamic recrystallization temperature by affecting grain boundary tortuosity and the degree of grain boundary embrittlement caused by impurity segregation. However, previous studies on the various factors influencing hot cracking, including the solidification mode, have predominantly focused on austenitic alloys such as stainless steels. This focus stems from the inherent susceptibility of the austenite phase to hot cracking compared to ferritic systems (including carbon steels), which is due to the extremely low solubility of impurities in austenite.

Recently, the authors observed the occurrence of hot cracking specifically, solidification cracking in the weld metal during high heat input submerged arc welding (SAW) of C-Mn steels utilized in the wind tower and shipbuilding industries. Consequently, efforts have been made to analyze the underlying causes and develop mitigation strategies. Although the alloying elements of the base metal influence the weld metal composition through dilution, in most cases, the occurrence of cracking was successfully prevented by selecting appropriate welding consumables, namely the wire or flux. The influence of alloying and impurity elements on the solidification cracking of carbon steels was first quantified in the early 1960s by J.C. Borland, who derived the Relative Potency Factor (RPF) based on the phase equilibria of binary alloys [3]. However, because the individual effect of each alloying or impurity element is interactive with other elements present in the alloy system, it is necessary to predict cracking susceptibility by considering the collective influence of all elements in a multicomponent system. In the mid to late 1970s, J.G. Garland and N. Bailey at The Welding Institute (TWI) developed an empirical formula for multicomponent weld metals using 17 cast steels combined with a single SAW wire and flux combination [4, 5]. This formula, known as the Units of Crack Susceptibility (UCS), categorizes weld metal compositions: a UCS value below 10 indicates low cracking susceptibility, whereas a value above 30 indicates high susceptibility. Although the UCS formula remains the most widely recognized empirical index for predicting solidification cracking in C-Mn steel weld metals, it has clear limitations. It was developed using cast materials based on fire-resistant and pressure vessel steels, thereby omitting the effects of microalloying and grain-refining elements commonly utilized in modern shipbuilding and wind tower steel grades.

In this study, the solidification cracking susceptibility was systematically evaluated using actual rolled plates rather than cast materials typically employed in the wind tower and shipbuilding industries, in combination with various commercial welding wires and fluxes of diverse chemical compositions. The thermodynamic equilibrium or partial equilibrium solidification temperature ranges, calculated as a function of alloying and impurity elements, were compared with the experimentally measured crack lengths and subsequently correlated with the calculated UCS numbers.

2. As-weld Crack analysis

In the production of heavy plates for wind structures or shipbuilding, the manufacturing process varies depending on customer requirements or applicable standards. Fig. 1 shows the schematic diagrams of (a) the normalizing or normalized rolling process and (b) the thermo-mechanical control process (TMCP), along with the microstructures of 320 MPa yield strength grade steels produced by each process. For normalized steels, the mechanical properties and microstructure are determined through normalizing heat treatment. Consequently, they require a higher addition of alloying elements compared to TMCP steels, which are manufactured through a complex combination of controlled rolling and accelerated cooling. Indeed, as shown in Fig. 1, a significant difference in microstructure is observed between the steels manufactured by the two processes. The normalized steel exhibits a mixed ferrite-pearlite structure (Fig. 1a), whereas the TMCP steel is characterized by a microstructure predominantly composed of fine ferrite (Fig. 1b). Reflecting these differences, the carbon equivalents (Ceq) calculated using the IIW formula show a substantial discrepancy, being approximately 0.40 for the normalized steel and 0.30 for the TMCP steel.



(a) (b)

Fig.1 Manufacturing process and Microstructure of (a)Normalized/Normalized Rolled, (b)TMCP Steels

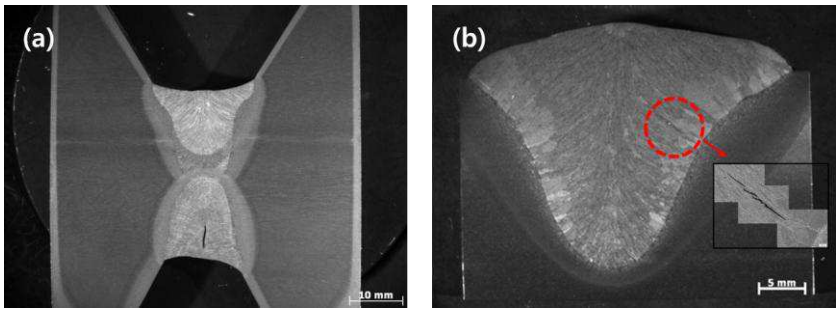


Fig.2 Weld metal cracking in wind tower and shipbuilding industries

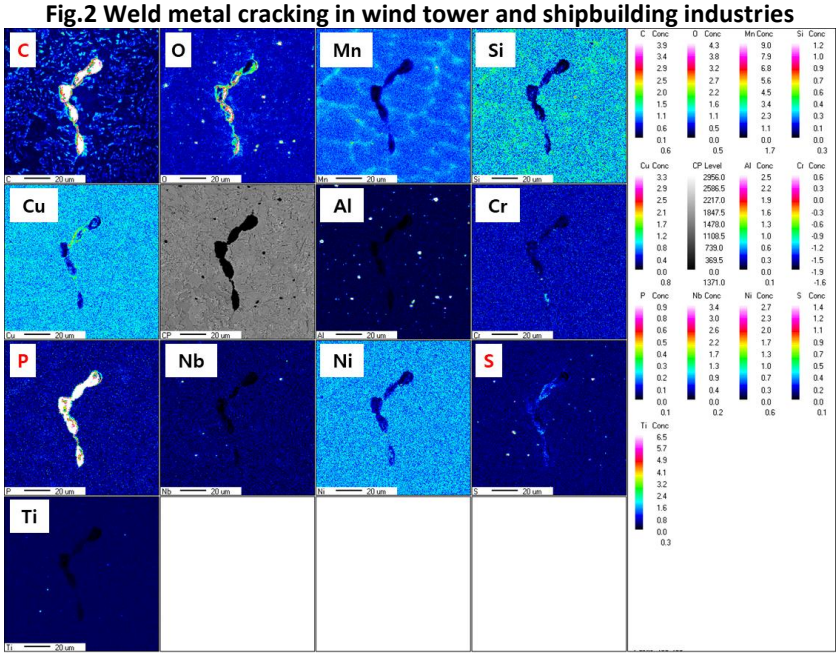


Fig.3 Segregation of alloying elements and impurities in secondary cracks

Such differences necessitate caution when fabricators weld steel plates that share the same strength grade but are manufactured via different processing routes. Typically, a fabricator's Welding Procedure Specification (WPS) is optimized for the specific steel grade they routinely use. If they switch to a steel plate produced by a different manufacturing process without modifying the WPS (such as adjusting the welding consumables), it can lead to a degradation of weldment toughness or the occurrence of cold and hot cracking. Fig. 2 illustrates cases of weld metal hot cracking encountered by wind tower and shipbuilding fabricators. Fig. 2a shows a typical solidification crack propagating along the centerline of the weld metal. In Fig. 2b, a flare-type crack, which initiated due to harsh welding conditions and unfavorable bead geometry, is observed. The fracture surfaces of both cases exhibited distinct dendritic features, confirming that the failures were indeed caused by solidification cracking.

In Fig. 2a, the first and second weld beads are deposited at the top, and the crack initiated in the third bead deposited on the backing side (bottom). The cause of this cracking can be attributed to the accumulation of constraint stresses arising from the asymmetric bead shape formed after the first and second passes, combined with the enrichment and segregation of alloying elements or impurities during multi-pass bead stacking. Fig. 3 presents the Electron Probe Microanalysis (EPMA) results, showing the segregation of alloying

elements near a secondary crack adjacent to the main crack in Fig. 2a. Intensive segregation of C, P, and S was observed in the vicinity of the crack, along with oxygen enrichment resulting from post-cracking oxidation. Although the segregation of other alloying/grain-refining elements and the formation of inclusions were also detected, carbon, phosphorus, and sulfur were confirmed to be the primary elements driving solidification cracking.

Table 1 lists the chemical compositions of the non-crack side (top of the specimen in Fig. 2a) and the crack side (bottom), measured using Spark Optical Emission Spectrometry (Spark-OES). Despite the application of identical welding consumables, the alloying elements were generally more enriched on the crack side than on the non-crack side. In particular, the carbon content showed a significant difference, measuring 0.106 wt.% on the non-crack side and 0.123 wt.% on the crack side, indicating that carbon enrichment played a pivotal role in cracking. Using the chemical compositions in Table 1, Fe-C quasi-binary diagrams for the non-crack (a) and crack (b) sides were constructed using Thermo-Calc (TCFE6 database: Steels/Fe-alloys v6.2). Both weld metal compositions exhibit a peritectic temperature of approximately 1483 °C. However, depending on their nominal carbon contents, the non-crack side (a) and the crack side (b) correspond to hypoperitectic and hyperperitectic compositions, respectively. Under the assumption of equilibrium solidification, the liquidus and solidus temperatures for both (a) and (b) are identical at 1515 °C and 1480 °C, respectively, yielding the same equilibrium solidification temperature range of 35 °C (Fig.4).

However, the phase transformation path during solidification differs significantly between the two compositions. For the hypoperitectic non-crack side (a), the transformation sequence is:

$L \rightarrow \delta + L \rightarrow \delta + \gamma \rightarrow \gamma$

whereas for the hyperperitectic crack side (b), it proceeds as:

$L \rightarrow \delta + L \rightarrow \gamma + L \rightarrow \gamma$

Unlike the non-crack side (a), where the $\delta \rightarrow \gamma$ transformation occurs after the liquid phase has completely solidified (i.e., in the solid state), the $\delta \rightarrow \gamma$ transformation in the crack side (b) occurs in the liquid-solid coexistence state. During the precipitation of the γ phase, impurity elements such as P and S, which have extremely low solubility in austenite, are rejected into the remaining liquid phase. This solute redistribution is expected to significantly lower the actual final solidification temperature of the crack side (b) [6]. Consequently, during the solidification of C-Mn steels, the peritectic temperature and composition dictate the temperature range of liquid-solid coexistence, thereby acting as critical factors governing solidification cracking susceptibility. In a previous study investigating the effect of a third alloying element (X) on the peritectic temperature and composition of Fe-C-X ternary alloys, it was reported that austenite stabilizers (e.g., Mn, Ni, Cu) raise the peritectic temperature, whereas ferrite stabilizers (e.g., Si, Cr, Mo, Ti) and impurities (P, S) lower it, thereby altering the carbon solubility in the liquid, γ, and δ phases at the peritectic temperature [7]. As the total alloy content increases, the $L+\delta+\gamma$ three-phase coexistence region widens, which is expected to further exacerbate hot cracking susceptibility.

	Chemical composition of weld metal (wt%)										
	C	Si	Mn	P	S	Cr	Ni	Cu	Al	Nb	Ti
None-crack Side	0.106	<0.5	<2.0	0.012	0.0027	<0.05	<0.1	<0.5	<0.05	<0.05	<0.01
Crack Side	0.123	<0.5	<2.0	0.014	0.0028	<0.05	<0.1	<0.5	<0.05	<0.05	<0.01

Table1. Chemical composition of the weld metal on non-crack(a) and crack(b) sides

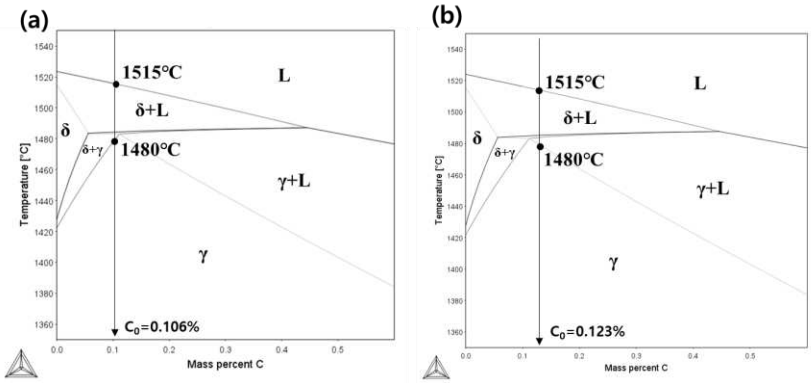


Fig.4 Quasi-binary phase diagrams for the weld metal compositions of the (a) non-crack and (b) crack sides

3. Analysis of solidification cracking susceptibility according to chemical composition

3.1 Fabrication of weld metals for evaluation

To evaluate the solidification behavior and subsequent cracking susceptibility as a function of chemical composition, three base metals, seven welding wires, and four welding fluxes were prepared. Their chemical compositions were analyzed using Inductively Coupled Plasma Optical Emission Spectrometry (ICP-OES). The major chemical compositions of the fluxes are listed in Table 2. The base metals were classified based on their carbon content into High C (0.3 wt.%), Medium C (0.16 wt.%), and Low C (0.08 wt.%). The manganese (Mn) content was up to 1.8 wt.%, while phosphorus (P) and sulfur (S) contents were in the ranges of 0.007–0.013 wt.% and 0.002–0.004 wt.%, respectively (Table 2a). Compositions other than these major elements, including microalloying elements, are omitted due to proprietary reasons. For the welding wires, seven commercial products were selected and categorized by carbon content into High C (0.13 wt.%), Med C (0.11 wt.%), and Low C (0.05 wt.%). Within each carbon category, the wires were further classified as High P, Low S, etc., based on their P and S contents. The Mn content of most wires was below 2.5 wt% except for Low C-Low Mn wire which contained 1.0 wt.% or less. All of the wires contained 1.0 wt.% nickel (Ni) or less. For the fluxes, four commercial products were selected with basicity indexes (BI) of 0.73, 1.76, 2.97, and 4.20. The basicity index was calculated using the formula presented in Table 2c [8].

To analyze the chemical compositions resulting from different combinations of base metals, welding wires, and fluxes, and to prepare specimens for Varestraint testing, Bead-on-Plate (BOP) SAW was performed on 20-

mm-thick steel plates. Under a heat input of approximately 8.5 kJ/mm, the base metal dilution ratio during BOP welding was analyzed to be approximately 65–75%. This is highly consistent with the 70% dilution ratio reported in the TWI studies [4, 5].

Table. 3 summarizes the chemical compositions of the 11 weld metals fabricated by BOP SAW. On the High C base metal, two weld metals (#1 and #2) were fabricated using combinations of one wire and one flux. On the Med C base metal, the following weld metals were prepared: two weld metals (#3 and #4) using one High C wire and two fluxes; two weld metals (#5 and #6) using a Med C-High P wire and two fluxes; and two weld metals (#7 and #8) using a Med C-Low P wire and two fluxes. Additionally, on the Low C base metal, weld metals were fabricated using a Low C wire and one flux (#9), a Low C-Low Mn wire and one flux (#10), and a combination of one wire and one flux (#11). Through comparative analysis of these combinations, the individual and combined effects of the base metal, wire, and flux on the chemical composition of the weld metal can be inferred. The carbon, phosphorus, and sulfur contents of the weld metals were primarily determined by the compositions of the base metal and the welding wire. Because the initial sulfur content of both the base metal and the welding consumables was extremely low, the sulfur content of the weld metals was also restricted to a narrow range of 0.003–0.005 wt.%.

By comparing cases where the base metal and wire were identical but the flux basicity differed (1.76 vs. 4.20), the influence of flux basicity on the C, P, and S contents can be elucidated (#3 to #8). When a flux with low basicity was used, the carbon content of the weld metal was consistently lower. This is attributed to the promotion of decarburization reactions driven by the high oxygen potential of low-basicity fluxes, which enhances the removal of carbon from the molten metal to the slag via the following reaction:

C+O=CO

Conversely, when a high-basicity flux was employed, the P and S contents in the weld metal could be reduced through dephosphorization and desulfurization reactions, which are represented as follows:

2P+5FeO+3CaO=3CaO·P2O5+5Fe or 2P+5FeO+4CaO=4CaO·P2O5+5Fe

S+CaO=CaS+O

In the present study, however, because the initial sulfur content of the base metal and welding consumables was already extremely low, only a consistent decrease in the phosphorus content was experimentally observed.

(a)

Concept	wt%			
	C	Mn	P	S
High C	0.3	<1.8	0.013	0.003
Medium C	0.16	<1.8	0.013	0.004
Low C	0.078	<1.8	0.007	0.002

(b)

Concept	wt%					
	C	P	S	Si	Mn	Ni
High C-High P	0.13	0.013	0.006	<0.05	<2.5	<1.0
High C-LowP-High S	0.13	0.0087	0.011	<0.05	<2.5	<1.0
Med C-HighP	0.11	0.019	0.0056	<0.05	<2.5	<1.0
Med C-Low P	0.11	0.012	0.0056	<0.05	<2.5	<1.0

Low C-High P	0.05	0.02	<0.02	<0.03	<2.5	<1.0
Low C-Low P	0.05	0.003	0.008	<0.05	<2.5	<1.0
Low C-Low Mn	0.05	<0.002	<0.02	<0.05	<1.0	<1.0

(c)

Basicity	**wt%**									
	CaF2	**CaO**	**MgO**	**Al2O3**	**SiO2**	**MnO**	**K2O**	**TiO2**	**Na2O**	**FeO**
0.73	<15	<1	<15	<45	<20	<5	<0.5	<6.5	<2.5	<7
1.76	-	<20	<30	<20	<20	<5	<1	<7	<2.5	<2
2.97	<25	<15	<35	<20	<15	<1	<0.5	<1.5	<1	<1
4.20	<40	<25	<30	<20	<15	<1.5	<1.5	<2	<1.5	<0.1

$BI = \{CaO + MgO + CaF_2 + Na_2O + K_2O + 1/2(MnO + FeO)\} / \{SiO_2 + 1/2(Al_2O_3 + TiO_2 + ZrO_2)\}$

Table2. Chemical composition of base metals(a), welding electrodes(b), and fluxs(c)

No.	Base metal	Wire	Flux	Chemical composition(wt%)					
				C	Si	Mn	P	S	Ni
1	High C	High C-High P	0.73	0.2	<0.5	<2.0	0.018	0.004	<1.0
2		Low C-Low P	2.97	0.18	<0.5	<2.0	0.009	0.003	<1.0
3	Med C	High C-Low P-High S	1.76	0.136	<0.5	<2.0	0.014	0.004	<1.0
4			4.20	0.14	<0.5	<2.0	0.013	0.004	<1.0
5		Med C-High P	1.76	0.133	<0.5	<2.0	0.017	0.003	<1.0
6			4.20	0.137	<0.5	<2.0	0.016	0.003	<1.0
7		Med C-Low P	1.76	0.135	<0.5	<2.0	0.014	0.003	<1.0
8			4.20	0.138	<0.5	<2.0	0.013	0.003	<1.0
9		Low C-High P	1.76	0.11	<0.5	<2.0	0.021	0.0054	<1.0
10		Low C-Low Mn		0.11	<0.5	<1.0	0.013	0.0054	<1.0
11	Low C	Med C-Low P	1.76	0.072	<0.5	<2.0	0.012	0.003	<1.0

Table3. Chemical composition of weld metals

3.2 Thermodynamic calculations for each alloy

To predict the solidification behavior of the weld metals, equilibrium and partial equilibrium calculations were performed using Thermo-Calc (TCFE6 database: Steels/Fe-alloys v6.2). Selected results are presented in Figs. 5–8. Unlike the conventional Scheil-Gulliver model, the partial equilibrium model accounts for the diffusion of interstitial elements (i.e., carbon) in the solid phase. Consequently, while the Scheil model is highly suitable for predicting the solidification behavior of high-alloy systems such as stainless steels, the partial equilibrium model is far more appropriate for C-Mn steels. Ultimately, comparing these thermodynamic calculations with experimental observations is the most effective approach for predicting the actual solidification temperature range.

Fig. 5 illustrates the equilibrium phase diagrams and the temperature-dependent phase transformation behavior calculated under partial equilibrium conditions for specimens #1, #2, and #11. For specimens #1 and #2, which were fabricated on the same High C base metal but with different welding consumables, the equilibrium calculations (Figs. 5a and 5b) predict hyperperitectic solidification behavior. The equilibrium

solidification temperature ranges (the difference between the liquidus and solidus temperatures) were calculated to be 55 °C and 46 °C, respectively. Under partial equilibrium conditions, however, the solidification temperature ranges widened to 130.5 °C and 104 °C, respectively, showing a significant discrepancy from the equilibrium results. Comparing specimens #1 and #2, the high carbon content of the base metal is identified as the primary driver of the hyperperitectic composition, whereas the higher C, P, and S contents of the welding wire used for specimen #1 (Figs. 5a and 5d) are responsible for its wider solidification temperature range. In contrast, specimen #11 (Figs. 5c and 5f), which was fabricated on the low-carbon base metal, exhibits hypoperitectic solidification behavior in the equilibrium calculation, with a narrower equilibrium solidification temperature range of approximately 37 °C compared to the hyperperitectic specimens #1 and #2. However, the partial equilibrium calculation reveals that the amount of primary δ-ferrite formed in specimen #11 is significantly larger than that in specimens #1 and #2. This extensive δ-ferrite formation leads to severe carbon segregation into the remaining liquid phase, which drastically lowers the final solidification temperature and consequently widens the solidification temperature range to 112 °C.

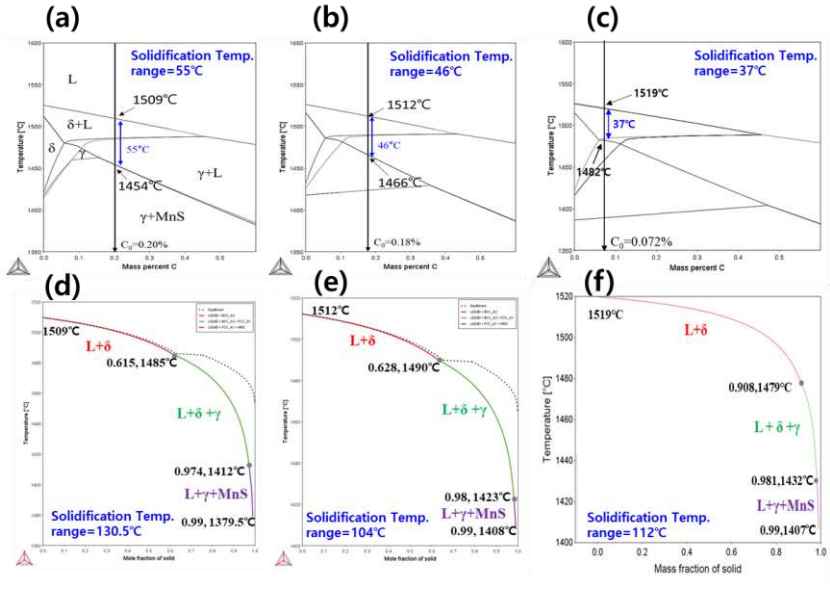


Fig.5 Equilibrium and partial equilibrium phase diagrams for specimens #1,2 and 11: (a),(d) for #1, (b),(e) for #2, and (d),(f) for #11

Fig. 6 depicts the segregation behavior of C, P, and S in the remaining liquid phase during solidification for specimens #1, #2, and #11. As solidification progresses, carbon and phosphorus continuously enrich in the liquid phase. In contrast, the sulfur content decreases during the final stage of solidification because it reacts with manganese to form MnS. Due to the lower C and P contents of the welding wire and the use of a high-basicity flux, specimen #2 exhibits lower concentrations of carbon and phosphorus in the final liquid phase than specimen #1 (Fig. 6b). Table 4 summarizes the nominal C and P compositions of specimens #1, #2, and #11, along with the C and P concentrations in the final liquid phase calculated via partial equilibrium. Regarding the carbon enrichment ratio in the remaining liquid phase, specimens #1 and #2 exhibit values of 4.4 and 4.8, respectively, whereas specimen #11 shows a significantly higher value of 7.4. This quantitative difference

confirms that the abundant formation of primary δ-ferrite during the solidification of specimen #11 promotes intense carbon segregation into the remaining liquid phase.

No. of specimen	Nominal C	Nominal P	Final C In Liquid	Final P In Liquid	C segregation (Final/Nominal)	P segregation (Final/Nominal)
1	0.2	0.018	0.878	0.751	4.4	41.7
2	0.18	0.009	0.86	0.337	4.8	37.4
11	0.072	0.012	0.535	0.428	7.4	35.7

Table4. Nominal and final composition of C, P in remained liquid by partial equilibrium calculation

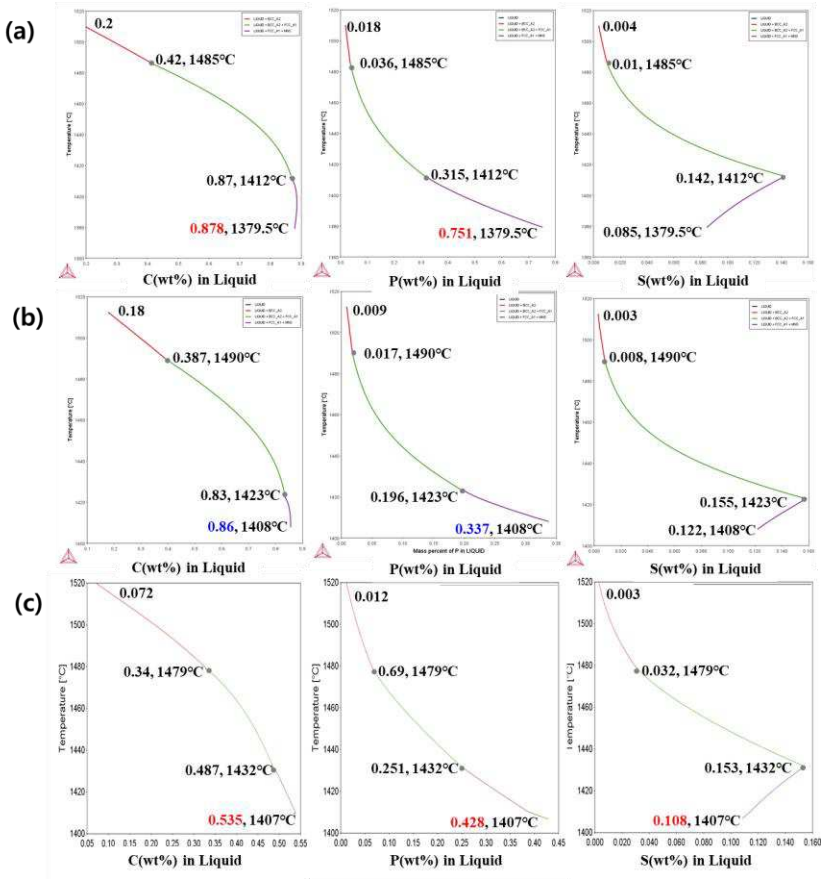


Fig.6 C, P, and S contents in the liquid calculated under partial equilibrium conditions for #1 (a), #2 (b), and #11 (c)

Figs. 7 and 8 show the equilibrium and partial equilibrium phase diagrams, as well as the segregation of C, P, and S in the remaining liquid phase during solidification, for weld metal specimens #3, #8, and #9, which were fabricated on the 0.16 wt.% Medium C base metal with different welding wires and fluxes. In the equilibrium phase diagrams, all three specimens exhibit hyperperitectic compositions. The solidification temperature ranges calculated under partial equilibrium conditions are 128.3 °C, 114.6 °C, and 107 °C for specimens #3, #8, and #9, respectively. Comparing specimens #3 and #8 (Figs. 7d, 8a and Figs. 7e, 8b, respectively), although specimen #3 was welded with a wire of higher carbon content than specimen #8, it

ended up with a similar weld metal carbon content due to the low-basicity flux used. However, due to its higher P and S contents, specimen #3 exhibits a wider solidification temperature range. Comparing specimens #3 and #9 (Figs. 7d, 8a and Figs. 7f, 8c, respectively), under the application of the same flux, specimen #9which utilized a low-carbon welding wire exhibits a narrower solidification temperature range.

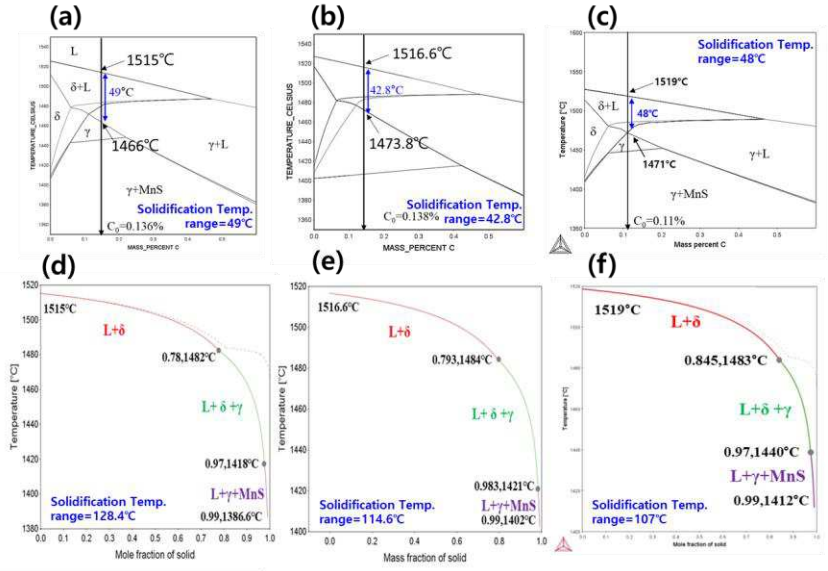


Fig.7 Equilibrium and partial equilibrium phase diagrams for specimens #3,8 and 9: (a),(d) for #3, (b),(e) for #8, and (d),(f) for #9

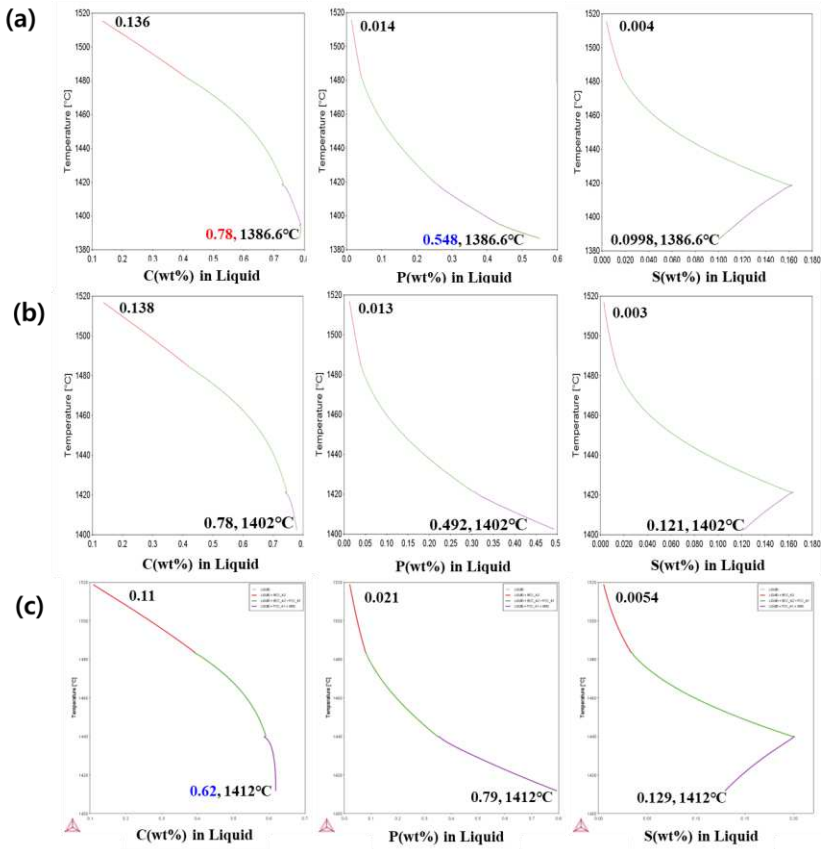


Fig.8 C, P, and S contents in the liquid calculated under partial equilibrium conditions for #3(a),8(b) and 9(c)

3.3 Evaluation and analysis of solidification cracking susceptibility

To evaluate the solidification cracking susceptibility of each weld metal, Transverse Varestraint tests were conducted. A Varestraint tester, as shown in Fig. 9, was utilized to control the amount of deformation applied to the specimens during welding by applying augmented strains ranging from 1% to 4%. The BOP weld specimens fabricated in Section 3.1 were prepared by positioning the weld bead in the center of the specimen (as shown in Fig. 10), removing and polishing the bead surface, and machining them into Varestraint test specimens. Gas Tungsten Arc Welding (GTAW) was then performed on the deposited weld metal in the transverse direction with a heat input of approximately 0.3 kJ/mm. The detailed welding parameters are summarized in Table 5. To measure the Brittle Temperature Range (BTR), the cooling rate was recorded during welding by installing an R-type thermocouple at the center of the weld bead on the Varestraint specimen.



Fig.9 Varestraint test setup with an augmented strain range of 1–4%

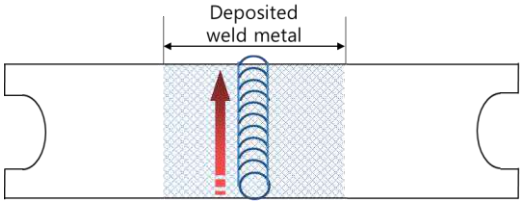


Fig.10 Varestraint test on the deposited weld metal

Welding Method	Current	Travel speed	Arc length	Gas	Heat input
Autogenous GTAW	100 A	4mm/sec	2 mm	Argon gas 20 L/ min	0.3 kJ/mm

Table5. Welding conditions for varestraint test

Fig. 11 shows the maximum crack length (MCL) and the calculated BTR values as a function of augmented strain for specimens #1, #2, and #11. The obtained BTRs were 64 °C, 55 °C, and 50 °C for specimens #1, #2, and #11, respectively. Specimen #1, which was predicted to have the widest solidification temperature range among all tested specimens, exhibited the longest MCL, with the crack length tending to saturate at an augmented strain of 2%. This indicates that a sufficient volume of liquid phase persists over a wide temperature

range, leading to the highest solidification cracking susceptibility. For the other specimens (excluding specimen #1), the MCL decreased significantly with decreasing carbon content. However, because the crack lengths did not fully saturate up to the maximum applied strain of 4%, the actual BTR values might be slightly higher. Each measured BTR value lies between the equilibrium and partial equilibrium calculated values, being closer to the equilibrium calculation results. Nevertheless, considering the significant influence of impurities such as P and S on the solidification temperature range, comparing the relative trends of the specimens using partial equilibrium calculations remains highly valid. Comparing the measured BTRs with the equilibrium and partial equilibrium calculation results, specimens #1 and #2 (high-carbon base metal) undergo the liquid-to-austenite (L→γ) and delta ferrite-to-austenite (δ→γ) transformations at the phase interfaces in the presence of a sufficient amount of liquid phase, resulting in a wide BTR (Figs. 5a, 5d, 11d and Figs. 5b, 5e, 11e). In contrast, for the low-carbon base metal (specimen #11), the δ→γ transformation occurs at the final stage of solidification, leading to a narrower BTR (Figs. 5c, 5f, 11f).

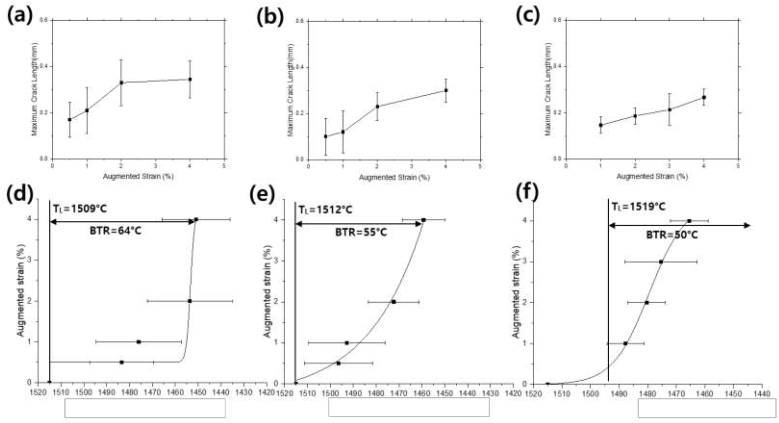


Fig.11 Results of varestraint tests and BTR of #1,2 and 11:
(a),(d) for #1, (b),(e) for #2, and (d),(f) for #11

Fig. 12 shows the MCL and BTR of specimens #3 to #8, fabricated on the 0.16 wt.% C medium-carbon steel, as a function of welding consumable changes. It was confirmed that the lower C and P contents of the welding wire reduced the crack length, and a higher flux basicity further mitigated cracking due to the dephosphorization effect. Comparing the BTRs of specimens #3, #8, and #9 with the equilibrium and partial equilibrium calculation results (Figs. 7a, 7d, 12d; Figs. 7b, 7e, 12e; and Figs. 7c, 7f, 12f, respectively), as the nominal composition approaches the peritectic composition (i.e., in the order of specimens #3, #8, and #9), the liquid-to-austenite transformation range becomes shorter, resulting in a narrower BTR.

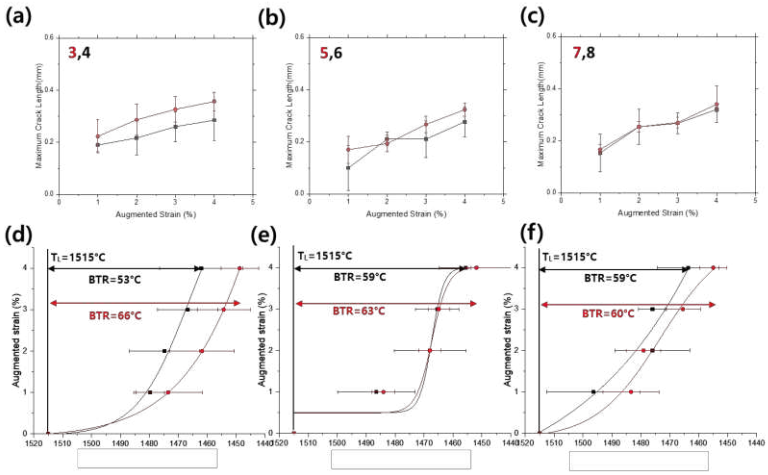


Fig.12 Results of varestraint tests and BTR of #3,4,5,6,7,8:
(a),(d) for #3 and 4, (b),(e) for #5 and 6, and (d),(f) for #7 and 8

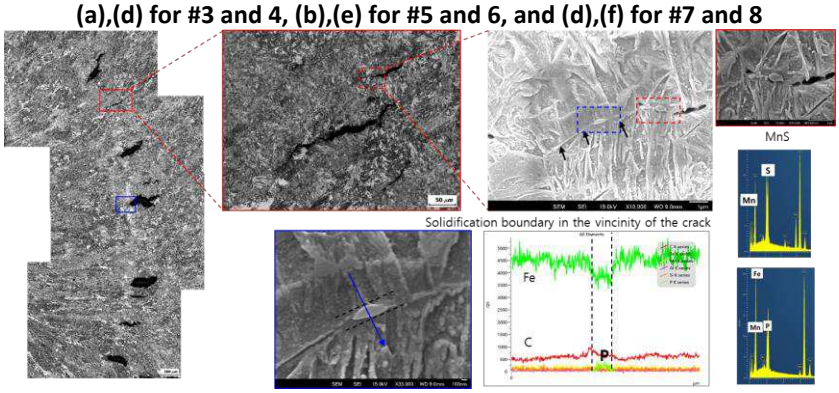


Fig.13. Evidence of impurity segregation in the vicinity of cracks in Varestraint specimens

Fig. 13 presents the Scanning Electron Microscope (SEM) and Energy Dispersive X-ray Spectroscopy (EDS) observation results of inclusion formation due to the segregation of P and S near the cracks of the tested specimen #5. The nominal C, P, and S compositions of this specimen were 0.13, 0.017, and 0.003 wt.%, respectively, while the calculated final liquid phase compositions were 0.77, 0.656, and 0.100 wt.%, respectively. The observation of MnS and phosphides confirms the severe segregation of these elements at the final solidification grain boundaries.

3.4 Summary of experimental results and discussion

Fig. 14 compares the calculated equilibrium solidification temperature range and the measured BTR (at 4% strain) of the weld metals investigated in this study as a function of carbon content. Both the equilibrium solidification temperature range and the BTR exhibit a clear upward trend with increasing carbon content. Furthermore, at a given carbon content, an increase in P and S contents also leads to an increase in both the equilibrium solidification temperature range and the BTR. Fig. 15 compares the correlation of the measured BTR with the UCS (Unit Crack Susceptibility) index and the partial equilibrium solidification temperature range. The results demonstrate that the partial equilibrium calculated values exhibit a stronger correlation with the

measured BTR than the UCS index. While several factors may contribute to this discrepancy, it is primarily attributed to differences in the alloy systems of the weld metals used in the respective studies, as well as differences in the crack length measurement methods following the Varestraint test. In TWI's SAW Varestraint test, the specimen is sectioned after testing to measure the crack length along the thickness direction. In contrast, in the present study, the pre-fabricated SAW weld metal was machined into thin plates for testing, and the lengths of the cracks propagating parallel to the welding direction were measured and directly compared with the BTR. Consequently, the correlation with the thermodynamically calculated solid-liquid coexistence range is superior to that of the UCS index.

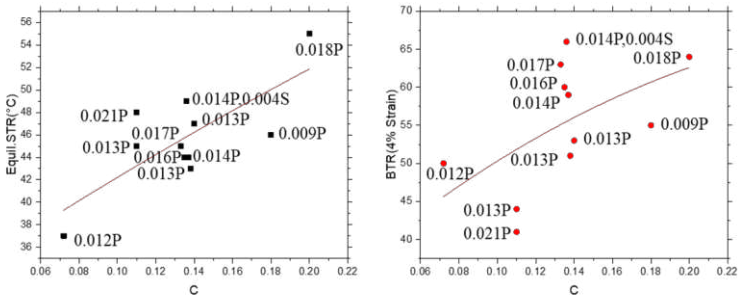


Fig.14. Calculated and measured cracking criteria as a function of C content for various P contents

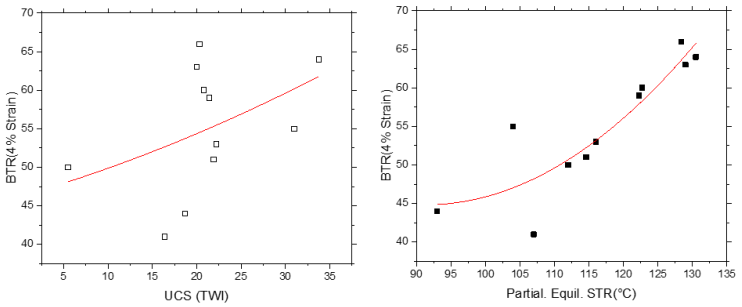


Fig.15. Correlation of UCS number and partial equilibrium solidification temperature range, compared with BTR from Varestraint tests

Fig. 16 maps the solidification cracking susceptibility of the C-Mn weld metals onto the Fe-C metastable phase diagram as a function of carbon content, which can be broadly categorized into three distinct regions. Region 1 corresponds to the composition range where excess delta ferrite remains after the peritectic reaction. In this region, phosphorus is partitioned into the delta ferrite, resulting in a low susceptibility to solidification cracking. Region 3 represents the high-carbon range where the peritectic reaction does not occur. As the carbon content increases, the final solidification temperature decreases, leading to a very high susceptibility to solidification cracking. Region 2, which is the primary focus of this study, is characterized by the presence of excess liquid remaining after the peritectic reaction. In this region, the solid–liquid coexistence range is governed predominantly by carbon and impurity elements; therefore, minimizing their contents is essential to mitigate solidification cracking susceptibility.

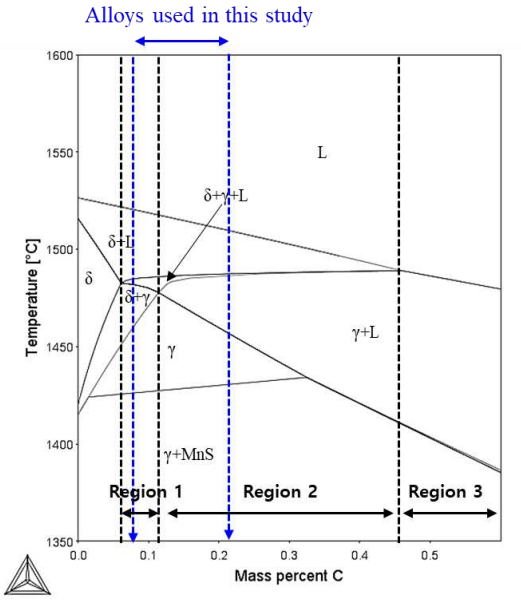


Fig.16. Solidification cracking susceptibility of C-Mn weld metals

4. Conclusions

To investigate the solidification cracking behavior of weld metals in heavy plates used for shipbuilding and wind towers, weld metals were fabricated using three types of base metals, seven types of welding wires, and four types of welding fluxes. The following conclusions were drawn through thermodynamic analyses of the solidification behavior for each composition and comparative evaluations of cracking susceptibility using Transverse Varestraint tests:

(1) The C, P, and S contents in the weld metals are directly proportional to the chemical compositions of the base metal and welding wire.

(2) The carbon content dominantly governs the solidification temperature range of the weld metals.

(3) The final solidification temperature decreases significantly due to the segregation and enrichment of phosphorus in the residual liquid phase during the austenite (γ) solidification stage.

(4) he effect of sulfur on the solidification temperature range is limited owing to its low nominal content and the preferential formation of MnS.

(5) A strong correlation in relative trends was observed between the measured BTR and the calculated solidification temperature ranges obtained from both equilibrium and partial equilibrium thermodynamic calculations.

Funding

The authors declare that no funds, grants, or other support were received during the preparation of this manuscript.

Competing Interests

The authors have no relevant financial or non-financial interests to disclose.

Author Contributions

Material preparation and experimental work were performed by K.Han and Y.Park. Data analysis was conducted by K.Han and S.Hong. The manuscript was written by K.Han, and all authors commented on the final version of manuscript.

5. References

[1] J. C. Lippold, Welding Metallurgy and Weldability. Hoboken, NJ, USA: John Wiley & Sons, 2015.
[2] S. Kou, Welding Metallurgy, 2nd ed. Hoboken, NJ, USA: John Wiley & Sons, 2003.
[3] J. C. Borland, "Suggested explanation of hot cracking in mild and low alloy steel welds," British Welding Journal, vol. 8, no. 11, pp. 526–540, 1961.
[4] J. G. Garland and N. Bailey, "Solidification cracking during the submerged-arc welding of carbon-manganese steels the effect of parent plate composition: carbon, manganese, sulphur, and phosphorus," Welding Research International, vol. 5, no. 3, pp. 1–33, 1975.
[5] J. G. Garland and N. Bailey, "Solidification cracking during submerged arc-welding of carbon-manganese steels detailed assessment of effect of parent plate compositions," Welding Research International, vol. 8, no. 3, pp. 240–281, 1978.
[6] A. Ghavam-Azizi, "Review of peritectic solidification mechanisms," Metallurgical and Materials Transactions B, vol. 51, pp. 1–15, 2020. (Note: Page numbers may vary depending on the specific online/print version).
[7] A. Kagawa and T. Okamoto, "Alloying elements and peritectic reaction in plain carbon steels," Materials Science and Technology, vol. 2, no. 11, pp. 1102–1108, 1986.
[8] S. S. Tuliani, N. F. Eaton, and T. Boniszewski, "Notch toughness of commercial submerged-arc weld metal," Welding and Metal Fabrication, vol. 37, no. 8, pp. 327–339, 1969.